Zeeman study of H^- local modes of Kramers rare-earth ions in CaF_2 and SrF_2

N. M. Strickland* and Glynn D. Jones
Department of Physics and Astronomy, University of Canterbury, PB 4800, Christchurch 8020, New Zealand
(Received 1 October 1999)

Splittings of the infrared absorption lines of doubly degenerate (X,Y) local-mode vibrations of H^- ions are observed for hydrogenic $C_{4v}H^-$ centers in CaF_2 and SrF_2 crystals containing Kramers rare-earth ions. These splittings are interpreted as electron–local mode phonon interaction effects in which the twofold degenerate (X,Y) local-mode vibrations, coupled to the Kramers-degenerate doublet electronic ground states of the rare-earth ions, are split into distinct doublets. The dominant contribution to these energy splittings comes from second order perturbation terms of the electron-phonon interaction. Nonlinear Zeeman shifts and splittings of the local mode lines can be quantitatively accounted for without introducing any additional parameters.

I. INTRODUCTION

The Zeeman splittings of vibronic lines of rare-earth (R^{3+}) ions in crystals are relatively little studied. The splitting patterns and relative intensities of the Zeeman components of most vibronic lines are the same as those of their electronic parent lines. As vibronic lines are often broad, such Zeeman components are not often observed.

For the case of the electron-phonon interaction between R^{3+} electronic states and localized molecular-type vibrations being larger than the Zeeman interaction, reductions occur in the Zeeman splittings[1] of the vibronic lines and their Zeeman components may have different relative-intensity patterns.[2] These vibronic Zeeman effects have been reported for U^{4+} ions in several host crystals.[1,2]

In CaF_2 and SrF_2 crystals containing trivalent rare-earth ions, H^- ions can serve as charge compensators. The principal hydrogenic rare-earth center produced is the tetragonal (C_{4v}) symmetry center in which the R^{3+} ion is charge compensated by an interstitial H^- ion located in the nearest-neighbor interstitial position, i.e., in the $\langle 100\rangle$ direction from the R^{3+} ion.[3] The coupling between the R^{3+} electronic states and the H^- local vibrational mode manifests itself both as an isotope shift in the R^{3+} electronic levels when D^- ions are substituted for H^- ions, and in the occurrence of vibronic transitions involving the local modes of the H^- or D^- ions. Such effects have been documented for H^- and D^- C_{4v} centers of Ce^{3+},[4] Pr^{3+},[5] Nd^{3+},[6] Gd^{3+},[3,7] Tb^{3+},[8] Er^{3+},[9–11] and Tm^{3+}.[12]

The motion of an H^- ion is not affected by a magnetic field and the g factors used for the analysis of Zeeman patterns of H^- local-mode lines are those of the parent R^{3+} electronic ground states. Nevertheless, the observed Zeeman patterns of the doubly-degenerate H^- (X,Y) local-mode lines are not simply identical to those of the R^{3+} electronic transitions. The four $H^-(X,Y)$ vibronic states are linear combinations of the doubly-degenerate R^{3+} electronic states and the doubly-degenerate $H^-(X,Y)$ local-mode states and these are not diagonal in the Zeeman interaction. The resulting Zeeman patterns differ markedly from those of the parent R^{3+} transitions and the effect of the H^- ion is more subtle than simply a Zeeman pattern displaced by the (X,Y) local-mode energy.

In this paper, we present Zeeman spectra that illustrate these vibronic-Zeeman effects for several Kramers ions in hydrogenic C_{4v} centers of CaF_2 and SrF_2. Kramers R^{3+} ions have odd-numbered $4f^n$ electron configurations and all their electronic states are at least twofold degenerate in the absence of an external magnetic field. Both electron-phonon and Zeeman splittings of the H^- (X,Y) local-mode lines occur for these R^{3+} ions. First, the H^- infrared-absorption lines are split into doublets by the electron-phonon interaction. These doublets are further split and shifted by applied magnetic fields to give non-linear Zeeman patterns.

Larger electron-phonon interaction splittings are observed for those ions whose excited electronic states have energies close to those of their respective (X,Y) local modes. Splittings of about 1 cm^{-1} were previously reported for the (X,Y) infrared-absorption lines of the H^-C_{4v} centers of Ce^{3+} in CaF_2 and SrF_2.[4] In this paper, we report (X,Y) splittings down to 0.2 cm^{-1} observed for H^- C_{4v} centers of other Kramers R^{3+} ions.

Of all the Kramers ions examined, Er^{3+} in CaF_2 shows more complex (X,Y) patterns because of the presence of an excited electronic level 4.5 cm^{-1} above the ground state.[9] Two (X,Y) splittings of 0.42 cm^{-1} and <0.2 cm^{-1} are observed, with the latter value being the splitting of the (X,Y) local mode line associated with the 4.5 cm^{-1} excited electronic level.

In applied magnetic fields, the (X,Y) local-mode lines are Zeeman split and shifted. Brief details of these Zeeman effects have been presented in conference reports.[13,14] Here we present and analyze the Zeeman-splitting patterns observed for Ce^{3+}, Nd^{3+}, Sm^{3+}, Dy^{3+}, Er^{3+}, and Yb^{3+} in CaF_2 and for Ce^{3+}, Nd^{3+}, and Sm^{3+} in SrF_2.

II. EXPERIMENTAL

The CaF_2 and SrF_2 crystals containing 0.01 to 0.05% of rare-earth trifluoride were grown from the melt in a A.D. Little R. F. 38 kW furnace by the Bridgman-Stockbarger method. Measurements were made on crystals which had been hydrogenated by heating the crystals in contact with molten aluminum at 850 °C in $\frac{2}{3}$ atmosphere pressure of hydrogen gas, typically for periods from 4 to 9 h. In the case of Yb^{3+} doping, the hydrogenation process has the additional

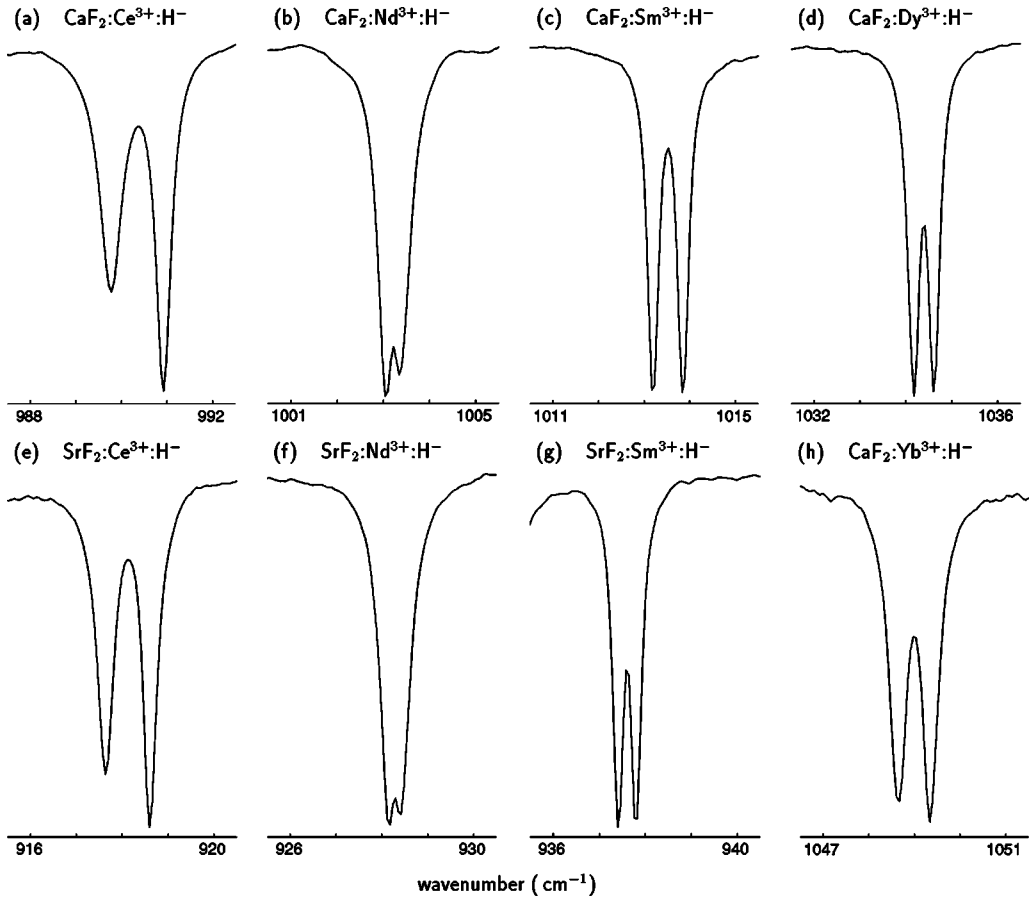

FIG. 1. 10 K infrared-absorption spectra of the split (X,Y) local-mode lines of the H^-C_{4v} centers of Kramers R^{3+} ions in CaF_2 and SrF_2.

effect of reducing the Yb^{3+} ions and periods of up to 40 h were required to get sufficient line intensities of the (X,Y) local modes. Quenching of the crystal samples to room temperature after hydrogenation minimized the formation of complex $R^{3+}-H^-$ cluster centers.

Infrared absorption spectra were measured at a resolution of 0.1 cm^{-1} using a Digilab FTS-40 FTIR spectrometer. Crystals were cooled to about 10 K by thermal contact using a Cryosystems LTS22.1 closed-cycle helium cryostat for zero field scans, or a liquid helium cryostat containing a 4 T Oxford Instruments superconducting magnet for Zeeman measurements. As the magnet is a simple solenoid, spectra were only measured with the magnetic field parallel to the optical axis, allowing the observation of σ polarized transitions only.

III. SPLITTING OF THE H^- (X,Y) LOCAL MODES BY THE ELECTRON-PHONON INTERACTION

Hydrogenation of CaF_2 and SrF_2 crystals containing R^{3+} ions results in the formation of several hydrogenic centers. Sharp lines due to H^- local modes of such centers appear in the infrared absorption spectra and have energies varying with the particular R^{3+} ion present.[3,15] For the principal H^-C_{4v} center, the H^- ion has C_{4v} site symmetry and two absorption lines, corresponding to the doubly degenerate (X,Y) and the nondegenerate Z local mode vibrations respectively, appear.[4] For all R^{3+} ions in CaF_2 and for R^{3+} ions up to Sm^{3+} in SrF_2, the lower frequency line is assigned as the (X,Y) mode of vibration and the higher frequency line as the Z mode.[3,15]

For Kramers R^{3+} ions in both CaF_2 and SrF_2 crystals below 77 K, the H^- (X,Y) local mode lines are sharp enough for (X,Y) splittings to be resolved into doublet components of equal intensity (Fig. 1), while the broader H^-Z local mode line remains unsplit.

A. The electron-phonon interaction

The observed splitting of the (X,Y) local-mode vibration is attributed to the coupling of these local-mode phonons to R^{3+} $4f$-electronic states by the electron-phonon interaction.[4,8,9] Because of the small mass of H^- compared to other ions of the crystal, the H^- local-mode phonon normal coordinates are simply X, Y, and Z, the displacements of the H^- ions from equilibrium. As R^{3+} crystal-field wave functions are usually expressed in a $|J,J_z\rangle$ basis, it is convenient to choose spherical-basis combinations of the phonon coordinates $X_\pm = \mp\sqrt{\frac{1}{2}}(X \pm iY)$. To terms quadratic in the H^- displacements, the electron-phonon interaction V_{ev} has the following form for C_{4v} symmetry:

$$V_{ev} = -(f_+X_- + f_-X_+) + f_zZ + g_{zz}Z^2 + g_{z-}X_+Z + g_{z+}X_-Z + g_+(X_+^2 + X_-^2) + g_-(X_+^2 - X_-^2) + g_{+-}X_+X_-,$$

where the electronic-coordinate functions f and g transform as the conjugate irreps to the respective phonon-coordinate

TABLE I. Electronic and vibrational states, their C_{4v} and C_4 irreps and their bases.

State	Group irrep		Basis states
	C_{4v}	C_4	
ψ^+	γ_6	μ_5	$\|\frac{1}{2}\rangle$, $\|-\frac{7}{2}\rangle$
ψ^-	γ_6	μ_6	$\|-\frac{1}{2}\rangle$, $\|\frac{7}{2}\rangle$
ϕ^+	γ_7	μ_7	$\|\frac{3}{2}\rangle$, $\|-\frac{5}{2}\rangle$
ϕ^-	γ_7	μ_8	$\|-\frac{3}{2}\rangle$, $\|\frac{5}{2}\rangle$
$[+]$	γ_5	μ_3	$-\sqrt{\frac{1}{2}}[(100)+i(010)]$
$[-]$	γ_5	μ_4	$\sqrt{\frac{1}{2}}[(100)-i(010)]$

functions and are related to the functions used previously and to the Racah-tensor operators $C_m^{(n)}$ by the following identities:

$$f_\pm = \mp\frac{1}{\sqrt{2}}(f_x \pm i f_y) = \sum_n \sqrt{\frac{(n+1)!}{2(n-1)!}} a_{1n}\langle r^n\rangle C_{\pm 1}^{(n)},$$

$$f_z = \sum_n a_{0n}\langle r^n\rangle C_0^{(n)},$$

$$g_+ = \frac{1}{2}(g_{xx}-g_{yy}) = \sum_n \frac{1}{8}\sqrt{\frac{(n+2)!}{(n-2)!}} b_{2n}\langle r^n\rangle (C_2^{(n)}+C_{-2}^{(n)}),$$

$$g_- = -\frac{1}{2} i g_{xy} = \sum_n \frac{1}{8}\sqrt{\frac{(n+2)!}{(n-2)!}} c_{2n}\langle r^n\rangle (C_2^{(n)}-C_{-2}^{(n)}),$$

$$g_{+-} = -(g_{xx}+g_{yy}) = \sum_n c_{0n}\langle r^n\rangle C_0^{(n)},$$

$$g_{zz} = \sum_n b_{0n}\langle r^n\rangle C_0^{(n)},$$

$$g_{z\pm} = \mp\frac{1}{\sqrt{2}}(g_{xz} \pm i g_{yz}) = \sum_n \pm\sqrt{\frac{(n+2)!}{2(n-2)!}} b_{1n}\langle r^n\rangle C_{\pm 1}^{(n)}.$$

The summations are over $n=2,4,6$ and the constants a_{0n}, a_{1n}, b_{0n}, b_{1n}, b_{2n}, c_{0n}, and c_{2n} depend on the particular model chosen for the $R^{3+}-H^-$ ion interaction. $\langle r^n\rangle$ are the $4f$ radial integrals for the particular R^{3+} ion.[16]

B. Point-charge model for the electron-phonon interaction

The form of the constants a_{1n}, b_{2n}, and c_{2n} have been derived[4,7] for several electrostatic models. For the analysis here, we adopt the simplest case of the point-charge model in which the interaction is between the point charge q of the hydrogenic ion and the R^{3+} $4f$ electron. For this point-charge model, the constants are

$$a_{0n} = -\frac{(n+1)eq}{4\pi\epsilon_0 D^{(n+2)}}, \quad b_{0n} = -c_{0n} = \frac{1}{2}\frac{(n+1)(n+2)eq}{4\pi\epsilon_0 D^{(n+3)}},$$

$$a_{1n} = \frac{eq}{4\pi\epsilon_0 D^{(n+2)}}, \quad b_{1n} = \frac{(n+2)eq}{4\pi\epsilon_0 D^{(n+3)}},$$

$$b_{2n} = c_{2n} = \frac{eq}{4\pi\epsilon_0 D^{(n+3)}},$$

where e is the charge of the $4f$ electron, q is the point charge of the hydrogenic ion and D is their separation. For CaF_2 and SrF_2, the values of $2D$ are the respective lattice constants 0.546 nm and 0.580 nm.

Attempts have been made to account for the observed frequencies of the (X,Y) and Z local modes for the H^-C_{4v} centers on an electrostatic model.[4,15] For CaF_2, both e and q were determined as 0.85 of an electronic charge[4] while for SrF_2 e and q were 0.98 of an electronic charge.[15]

C. (X,Y) vibronic states for Kramers ions

The electronic wave functions of any Kramers R^{3+} ions located in C_{4v} symmetry sites are either γ_6 or γ_7 doublets, with their components transforming as particular irreps μ_i of the C_4 group.

For the ground states, we distinguish these two possibilities by labelling these states $\psi^\pm$ for γ_6 ground states and $\phi^\pm$ for γ_7 ground states. Their C_4 group decompositions and representative $|J_z\rangle$ basis functions are given in Table I.

The (X,Y) local-mode states (100) and (010) transform as a γ_5 doublet of C_{4v}, with its components $[\pm] = \mp\sqrt{\frac{1}{2}}[(100)\pm i(010)]$, transforming as the μ_3 and μ_4 irreps of C_4 (Table I).

When either of the ground states, $\psi^\pm$ or $\phi^\pm$, is combined with the γ_5 symmetry vibration doublet $[\pm]$, two vibronic doublets of symmetry γ_6 and γ_7 are produced. The (X,Y) local-mode vibronic states will be labeled $\Psi_6^\pm$ and $\Psi_7^\pm$ for $\psi^\pm$ electronic ground states and $\Phi_6^\pm$ and $\Phi_7^\pm$ for $\phi^\pm$ electronic ground states, where the subscript denotes the C_{4v}

TABLE II. Vibronic states of ground and excited-electronic states and the $f_\pm$ electronic operators with their C_{4v} and C_4 irreps.

Irreps		Electronic	(X,Y) vibronic states		Intermediate states		$f_\pm$ operators	
C_{4v}	C_4	states	Ψ	Φ	(000)	(110)	$f\psi$	$f\phi$
γ_6	μ_5	ψ^+	$\Psi_6^+ = \psi^-[+]$	$\Phi_6^+ = \phi^-[-]$	$\psi^+(000)$	$\phi^+(110)$	$f_+\psi^-$	$f_-\phi^-$
γ_6	μ_6	ψ^-	$\Psi_6^- = \psi^+[-]$	$\Phi_6^- = \phi^+[+]$	$\psi^-(000)$	$\phi^-(110)$	$f_-\psi^+$	$f_+\phi^+$
γ_7	μ_7	ϕ^+	$\Psi_7^+ = \psi^-[-]$	$\Phi_7^+ = \phi^-[+]$	$\phi^+(000)$	$\psi^+(110)$	$f_-\psi^-$	$f_+\phi^-$
γ_7	μ_8	ϕ^-	$\Psi_7^- = \psi^+[+]$	$\Phi_7^- = \phi^+[-]$	$\phi^-(000)$	$\psi^-(110)$	$f_+\psi^+$	$f_-\phi^+$

irrep of the product state. The wave function composition and C_4 irreps of these vibronic states are included in Table II.

We consider perturbations of these vibronic states by the electron-phonon interaction for cases where the electronic ground state can be considered well separated from other electronic states. The exception is $CaF_2:Er^{3+}$ which is considered separately in Sec. IV B.

The different energies of the respective vibronic states constitute the (X,Y) splitting of the (100), (010) vibronic level.

D. First-order perturbation contributions to an (X,Y) splitting

In first-order perturbation, the first degree electron-phonon terms $(f_+X_- + f_-X_+)$ give zero matrix elements between the four vibronic states. These first-degree terms can only connect states differing by one vibrational quantum.

In first-order perturbation, second-degree electron-phonon terms have diagonal matrix elements only, since the four vibronic wave functions transform as different C_4 irreps (Table II). The only second-degree electron-phonon terms in which both the electronic and vibrational parts transform as γ_1 are $(g_{+-}X_+X_- + g_{ZZ}Z^2)$. Matrix elements of these terms are identical for each of the four vibronic states, resulting only in a uniform shift with no net contribution to any (X,Y) splitting.

E. Second-order perturbation contributions to an (X,Y) splitting

.

In second-order perturbation, the first-degree electron-phonon term f_zZ has nonzero matrix elements, but produces a uniform shift of all vibronic states with no net (X,Y) splitting.

The first-degree terms $(f_+X_- + f_-X_+)$ have electronic and vibrational parts that transform as the conjugate irreps $\gamma_5\mu_3/\gamma_5\mu_4$ (Table II). Hence they connect the four vibronic states to different intermediate states, producing independent shifts for the γ_6 and γ_7 vibronic states and thus a net (X,Y) splitting.

The major contribution to the (X,Y) splitting is from the $(f_+X_- + f_-X_+)$ terms in second-order perturbation.

The required intermediate vibronic states involved in these second-order perturbation energy shifts necessarily transform as the same irreps γ_6 or γ_7 as the ground-state (X,Y) vibronic states and involve the vibrational states (000), (110), and $\sqrt{\frac{1}{2}}[(200)\pm(020)]$, which all differ by one vibrational quantum from (100) or (010). Since the $\sqrt{\frac{1}{2}}[(200)\pm(020)]$ states are nearly degenerate compared to the local-mode energy, the intermediate states involving these contribute essentially a uniform shift, with no net (X,Y) splitting. Hence, we need consider only the intermediate vibronic product states of excited electronic states and the (000) or (110) vibrational states. The possible combinations are listed in Table II according to their C_4 irreps.

The excited electronic state components of these intermediate vibronic states are distinguished by representing the γ_6 states by $\psi_i^{\pm}$ and the γ_7 states by $\phi_i^{\pm}$. These electronic states are connected by the operators $f_{\pm}$ to the ground electronic states. Table II gives the irreps of $f\psi$ and $f\phi$ for identifying these connections.

For a γ_6 ground state, the (X,Y) vibronic states $\Psi_6^{\pm}$ and $\Psi_7^{\pm}$ have second-order perturbation shifts given by

$$E_{\Psi_6} = \alpha^2 \sum_i \frac{|\langle \psi_i^+ | f_+ | \psi^- \rangle|^2}{\hbar\omega_x - \epsilon_{\psi_i}} + \alpha^2 \sum_i \frac{|\langle \phi_i^+ | f_- | \psi^- \rangle|^2}{-\hbar\omega_x - \epsilon_{\phi_i}},$$

$$E_{\Psi_7} = \alpha^2 \sum_i \frac{|\langle \phi_i^+ | f_- | \psi^- \rangle|^2}{\hbar\omega_x - \epsilon_{\phi_i}} + \alpha^2 \sum_i \frac{|\langle \psi_i^+ | f_+ | \psi^- \rangle|^2}{-\hbar\omega_x - \epsilon_{\psi_i}},$$

where $\alpha = \sqrt{\hbar/2m\omega_x}$ is the amplitude of the $H^-(X,Y)$ local-mode vibration and the energy of the (110) local-mode state is $2\hbar\omega_x$.

For a γ_7 ground state, the (X,Y) vibronic states $\Phi_6^{\pm}$ and $\Phi_7^{\pm}$ have second-order perturbation shifts given by

$$E_{\Phi_6} = \alpha^2 \sum_i \frac{|\langle \psi_i^+ | f_- | \phi^- \rangle|^2}{\hbar\omega_x - \epsilon_{\psi_i}} + \alpha^2 \sum_i \frac{|\langle \phi_i^+ | f_+ | \phi^- \rangle|^2}{-\hbar\omega_x - \epsilon_{\phi_i}},$$

$$E_{\Phi_7} = \alpha^2 \sum_i \frac{|\langle \phi_i^+ | f_+ | \phi^- \rangle|^2}{\hbar\omega_x - \epsilon_{\phi_i}} + \alpha^2 \sum_i \frac{|\langle \psi_i^+ | f_- | \phi^- \rangle|^2}{-\hbar\omega_x - \epsilon_{\psi_i}}.$$

The second-order perturbation energy shifts are largest when the energy differences, $(\hbar\omega_x - \epsilon_{\psi_i})$ or $(\hbar\omega_x - \epsilon_{\phi_i})$, in the denominators becomes small. These occur for those intermediate vibronic states formed from (000) phonon states. Those R^{3+} ions with excited electronic states having energies ϵ_{ψ_i} or ϵ_{ϕ_i} close to $\hbar\omega_x$ will exhibit the largest (X,Y) splittings.

IV. SPLITTINGS OF (X,Y) LOCAL MODES OF H^-C_{4v} CENTERS

A. (X,Y) splitting for H^-C_{4v} centers in CaF_2 and SrF_2

The infrared-absorption spectra of (X,Y) splittings for several Kramers R^{3+} ions are shown in Fig. 1 and the measured (X,Y) splittings are included in Table III along with the electron-phonon parameters calculated for the choice of $q=e=0.85$ of an electronic charge[4] for CaF_2 and $q=e=0.9$ of an electronic charge for SrF_2 and for host-lattice values for D of 0.273 nm for CaF_2 and 0.290 nm for SrF_2.

The point-charge model calculation of the (X,Y) splitting requires that the energies and wave functions of those intermediate states closest in energy to the (X,Y) vibration be known or estimated. Where crystal-field energies were not available for the H^-C_{4v} centers, those for the F^-C_{4v} centers were adopted as being a close approximation. Crystal-field wave functions were calculated either from reported crystal-field parameters, or by fitting to the reported energy levels. The citation source in each case is given in Table IV.

$CaF_2:Ce^{3+}$ and $SrF_2:Ce^{3+}$

As no data has been reported on the excited states of the H^-C_{4v} centers, the crystal-field energies of the F^-C_{4v} centers were adopted. The ground-state g values[17–19] for these two centers differ by less than 5%, so this can be regarded as

TABLE III. Calculated values for the electron-phonon interaction parameters $a_{1n}\langle r^n\rangle\alpha$ on the point charge model for several Kramers ions in CaF_2 and SrF_2. Effective point charges $q=e$ of 0.85e and 0.9e and host-lattice distances D of 0.273 and 0.290 nm are adopted for CaF_2 and SrF_2, respectively.

Host	R^{3+}	Electron-phonon parameters (cm^{-1})			(X,Y) splittings (cm^{-1})	
		$a_{12}\langle r^2\rangle\alpha$	$a_{14}\langle r^4\rangle\alpha$	$a_{16}\langle r^6\rangle\alpha$	Calculated	Measured
CaF_2	Ce^{3+}	65.76	7.08	1.63	2.64	1.15
	Nd^{3+}	54.56	4.89	0.94	0.18	0.3
	Sm^{3+}	47.86	3.85	0.67	4.17	0.67
	Dy^{3+}	38.97	2.65	0.38	0.14	0.42
	Er^{3+}	35.8	2.27	0.30	$\cdots$(see Table V)$\cdots$	
	Yb^{3+}	32.65	1.91	0.23	0.12	0.70
SrF_2	Ce^{3+}	60.25	5.71	1.17	2.33	0.95
	Nd^{3+}	49.92	3.99	0.68	0.15	0.2
	Sm^{3+}	43.81	3.12	0.48	1.75	0.38

a reasonable approximation. A similar adoption of F^-C_{4v} center data was used for the Sm^{3+} and Yb^{3+} calculations. The discrepancy between the calculated and measured (X,Y) splittings for both $CaF_2:Ce^{3+}$ and $SrF_2:Ce^{3+}$ is about a factor of two, which is reasonable given the approximations inherent in the point-charge model.

$CaF_2:Nd^{3+}$ and $SrF_2:Nd^{3+}$

In this case the (X,Y) splittings are just resolved at the available resolution. The discrepancies between measured and calculated values of the splittings were less than in the case of Ce^{3+}.

$CaF_2:Sm^{3+}$ and $SrF_2:Sm^{3+}$

The measured and calculated (X,Y) splittings are not in good agreement in this case. We believe the reason for this is the ${}^6H_{3/2}$, ψ_1 state. For the F^-C_{4v} center in $CaF_2:Sm^{3+}$, the energy of this state is calculated to be 985 cm^{-1}, just 28 cm^{-1} from the (X,Y) local mode, and the exact energy of this state in the H^-C_{4v} center is critical. This one intermediate state contributes 4.14 cm^{-1} to the calculated (X,Y) splitting of 4.17 cm^{-1} which must therefore be considered very approximate.

For the H^-C_{4v} center of $SrF_2:Sm^{3+}$, the energy of the (X,Y) local mode has shifted to the lower energy side of the ψ_1 electronic state and is at 938 cm^{-1}. This ψ_1 state now pushes the $\Psi_6^{\pm}$ vibronic down in energy rather than up and the order of the two doublet vibronics is the reverse of the CaF_2 case. The Z local-mode line also appears in the infrared absorption spectrum of $SrF_2:Sm^{3+}$ [Fig. 1(g)], at lower energy than the (X,Y) line.

$CaF_2:Gd^{3+}$

No resolvable (X,Y) splittings were observed for the H^-C_{4v} center of $CaF_2:Gd^{3+}$, which was expected since Gd^{3+} has only a very small zero-field splitting for its ${}^8S_{7/2}$ ground multiplet, through second-order mixing with the ${}^6P_{7/2}$ and higher multiplets above 30 000 cm^{-1}.

$CaF_2:Dy^{3+}$

No data has been reported on the electronic levels of the H^-C_{4v} center in $CaF_2:Dy^{3+}$. For the parent F^-C_{4v} center, several optical studies have been reported,[20–23] with much disagreement on the assignment of centers. It was found[24] that no EPR resonances were observed for any tetragonal centers in $CaF_2:Dy^{3+}$.

The crystal-field parameters (all in cm^{-1}) used for the analysis here of the (X,Y) splitting were estimated by interpolation between those for F^-C_{4v} centers[8,25] of Tb^{3+} and

TABLE IV. Electronic ground-state g values, and references for excited state wave functions and energies used in the (X,Y) splitting calculations.

Host	R^{3+}	Ground-state g values				Crystal field
		Irrep	$g_\parallel$	$g_\perp$	Reference	Reference
CaF_2	Ce^{3+}	γ_7	3.150	1.330	H^- [17,18]	F^- [19,28]
	Nd^{3+}	γ_6	4.80	0.967	H^- [6]	H^- [6]
	Sm^{3+}	γ_6	<0.1	0.868	H^- [17]	F^- [29]
	Dy^{3+}	γ_7	17.2	0.036	(calculated)	(interpolated)
	Yb^{3+}	γ_7	2.412	3.802	F^- [30]	F^- [31]
	Er^{3+} (Z_1)	γ_7	7.465	6.1	H^- [9]	H^- [10]
	(Z_2)	γ_6	1.683	9.09		
SrF_2	Ce^{3+}	γ_7	2.854	1.472	F^- [32,33]	F^- [28]
	Nd^{3+}	γ_6	4.275	1.507	F^- [6]	H^- [6]
	Sm^{3+}	γ_6	<0.1	0.862	H^- [34]	F^- [29]

Ho^{3+}. The calculated ground-state wave function $\phi^{\pm} = 0.992|\pm\frac{13}{2}\rangle + 0.107|\pm\frac{5}{2}\rangle$ has $g_{\parallel} = 17.12$ and $g_{\perp} = 0.036$. The form of the ground-state wave function explains the absence of an observed EPR resonance for the $F^- C_{4v}$ center. EPR resonance transitions require $\Delta J_z = 0, \pm 1$ selection rules. With the calculated wave function having only < 0.1 of both $|\mp\frac{3}{2}\rangle$ and $|\mp\frac{11}{2}\rangle$ components, any EPR transition would be weak. Related to this is the low value of $g_{\perp}$.

CaF_2:Yb^{3+}

Yb^{3+} is readily reduced to the divalent Yb^{2+} form, especially in the hydrogenation process where the aluminum metal acts as reducing agent. Because of this, the $H^- C_{4v}$ center of Yb^{3+} is difficult to produce at the same concentration as those of other rare-earth ions and the vibrational modes of this center were not reported in the earliest work.[3] Subsequently, a pattern of four H^- local mode lines were reported.[26]

In the 10 K infrared absorption spectra of CaF_2:Yb^{3+} measured here, only one line that could be attributed to the (X,Y) local mode was observed. When measured at 0.1 cm^{-1} resolution, this line showed the doublet splitting of (X,Y) local-mode lines, in this case a splitting of 0.70 cm^{-1} [Fig. 1(h)]. The behavior of this line in a magnetic field (Sec. VI B) was also entirely consistent with it being the (X,Y) line of the $H^- C_{4v}$ center of Yb^{3+}.

B. *(X,Y)* splitting for $H^- C_{4v}$ centers in CaF_2:Er^{3+}

The splitting of the (X,Y) local-mode lines of the $H^- C_{4v}$ center in CaF_2:Er^{3+} is complicated by the presence of a low-lying first excited γ_6 state 4.5 cm^{-1} above the γ_7 ground state. In accordance with the adopted notation these two states are labeled $\psi^{\pm}$ and $\phi^{\pm}$, respectively, with their (X,Y) vibronics labeled according to Table II.

At the 10 K temperature of measurement of the infrared absorption spectrum, this first excited state is significantly populated and local-mode lines associated with both the ground state and the first excited state are seen in the already-published spectrum of CaF_2:Er^{3+}.[13] These two local-mode lines are separated by 1.47 cm^{-1}. Their temperature-dependent intensities show that the lower-energy (X,Y) line at 1037.85 cm^{-1} is associated with the Z_1 ground state and the higher-energy line at 1039.32 cm^{-1} with the Z_2 first excited state.[13] The (X,Y) local-mode line associated with the Z_1 state has an (X,Y) splitting of 0.42 cm^{-1}, while the (X,Y) splitting associated with the Z_2 state shows a flattened profile indicative of incipient splittings ≈ 0.1 cm^{-1}.

The vibronic transitions $Z_2(000) \rightarrow Z_1[\pm]$ and $Z_1(000) \rightarrow Z_2[\pm]$ are weak and acquire their intensities by electron-phonon admixtures between the Ψ and Φ vibronic states.

With the low-lying Z_2 electronic level present, extra contributions to (X,Y) splittings occur through both first and second-order perturbation. Calculations are presented here with point-charge model values for the several electron-phonon interaction parameters involved.

1. First-order perturbation shifts

First-order perturbation shifts arise from the second-degree terms $g_{+-}X_+X_-$, $g_{zz}Z^2$, and $g_{\pm}(X_+^2 \pm X_-^2)$ in the electron-phonon interaction. The energy matrix formed between the vibronic states of the Z_1 state ψ and the Z_2 state ϕ has diagonal matrix elements in first-order perturbation which differ for the Ψ and Φ states giving a shift in the two local-mode energies. There are also off-diagonal matrix elements connecting states with the same C_4 irrep label (Table II).

The perturbation energy matrix is

	$\phi^-[+]$	$\phi^+[-]$	$\phi^-[-]$	$\phi^+[+]$	$\psi^-[+]$	$\psi^+[-]$	$\psi^-[-]$	$\psi^+[+]$
$\phi^-[+]$	$-\Delta+E_1$						$A-B$	
$\phi^+[-]$		$-\Delta+E_1$						$A-B$
$\phi^-[+]$			$-\Delta+E_1$		$A+B$			
$\phi^+[+]$				$-\Delta+E_1$		$A+B$		
$\psi^-[+]$			$A+B$		$\Delta+E_2$			
$\psi^+[-]$				$A+B$		$\Delta+E_2$		
$\psi^-[-]$	$A-B$						$\Delta+E_2$	
$\psi^+[+]$		$A-B$						$\Delta+E_2$

where 2Δ is the splitting between the electronic states $\psi^{\pm}$ and $\phi^{\pm}$ of 4.5 cm^{-1}.

The various terms of this matrix are

$$E_1=(2\alpha^2-\beta^2)\langle\phi^+|g_{+-}|\phi^+\rangle=(2\alpha^2-\beta^2)b_{0n}\langle\phi^+|C_0^{(n)}|\phi^+\rangle,$$

$$E_2=(2\alpha^2-\beta^2)\langle\psi^+|g_{+-}|\psi^+\rangle=(2\alpha^2-\beta^2)b_{0n}\langle\psi^+|C_0^{(n)}|\psi^+\rangle,$$

$$A=2\alpha^2\langle\psi^+|g_+|\phi^+\rangle=2\alpha^2 b_{2n}\langle\psi^+|(C_2^{(n)}+C_{-2}^{(n)})|\phi^+\rangle,$$

$$B=-2\alpha^2\langle\psi^+|g_+|\phi^+\rangle=2\alpha^2 c_{2n}\langle\psi^+|(C_2^{(n)}-C_{-2}^{(n)})|\phi^+\rangle,$$

where we have assumed a point-charge model for which Laplace's relation gives $g_{+-}=-g_{zz}$ (equivalently $b_{0n}=-c_{0n}$) and

$$\langle[\pm]|X_+X_-|[\pm]\rangle=2\alpha^2,$$

$$\langle[\pm]|Z^2|[\pm]\rangle=\beta^2,$$

$$\langle[\mp]|(X_+^2+X_-^2)|[\pm]\rangle=2\alpha^2,$$

$$\langle[\mp]|(X_+^2-X_-^2)|[\pm]\rangle=\mp 2\alpha^2,$$

where β is the amplitude $\sqrt{\hbar/2m\omega_z}$ of the Z local-mode vibration of the H^- ion.

Using the crystal-field wave functions and point-charge model values for the second-degree coefficients appropriate for Er^{3+} the matrix-element terms (in cm^{-1}) are

$$E_1=-0.18,\quad E_2=0.83,\quad A=0.054,\quad \text{and}\quad B=0.182,$$

with the perturbation-matrix eigenvalues (in cm^{-1}) being -2.440, -2.433, 3.083, and 3.090.

2. Second-order perturbation shifts

Second-order perturbation shifts arise from the first-degree terms $(f_+X_-+f_-X_+)$ and f_ZZ of the electron-phonon interaction. Second-order perturbations from these first-degree terms connecting to intermediate states involving (000) and (110) local-mode states arise just as with the other Kramers ions. In addition, the contributions arising from the f_zZ term to the $[(101)\pm i(011)]$ intermediate states and the $(f_+X_-+f_-X_+)$ terms to the $[(200)\pm(020)]$ intermediate states yield different shifts for the Ψ and Φ states.

Furthermore, the second excited Z_3 level at 25.8 cm^{-1} above Z_1 is sufficiently close in energy to contribute in second-order perturbation.

For the $\Phi_6^{\pm}$ and $\Phi_7^{\pm}$ vibronics, these second-degree shifts are identical at

$$\Delta\epsilon(\Phi_6)=\Delta\epsilon(\Phi_7)=\frac{|\langle\phi_i^-[-]|g_{+-}(X_++X_-)+g_{zz}Z^2|\phi^-[-]\rangle|^2}{\epsilon_\phi-\epsilon_{\phi_i}}=\frac{(2\alpha^2-\beta^2)(b_{12}\langle r^2\rangle)^2\langle\phi_i^-|C_0^{(2)}|\phi^-\rangle|^2}{\epsilon_\phi-\epsilon_{\phi_i}}.$$

For the $\Psi_6^{\pm}$ vibronics the shift is

$$\Delta\epsilon(\Psi_6)=\frac{|\langle\phi_i^-[-]|g_+(X_+^2+X_-^2)+g_-(X_+^2-X_-^2)|\psi^-[+]\rangle|^2}{\epsilon_\psi-\epsilon_{\phi_i}}=\frac{16\alpha^4(b_{12}\langle r^2\rangle)^2\langle\phi_i^-|C_2^{(2)}|\psi^-\rangle|^2}{\epsilon_\psi-\epsilon_{\phi_i}}.$$

For the $\Psi_7^{\pm}$ vibronics the shift is

$$\Delta\epsilon(\Psi_7)=\frac{|\langle\phi_i^-[+]|g_+(X_+^2+X_-^2)+g_-(X_+^2-X_-^2)|\psi^-[-]\rangle|^2}{\epsilon_\psi-\epsilon_{\phi_i}}=\frac{16\alpha^4(b_{12}\langle r^2\rangle)^2\langle\phi_i^-|C_{-2}^{(2)}|\psi^-\rangle|^2}{\epsilon_\psi-\epsilon_{\phi_i}}.$$

For the point-charge model values for the second-degree electron-phonon parameters $b_{12}\langle r^2\rangle\alpha$, these terms shift the vibronic states Φ_6, Φ_7, Ψ_6, and Ψ_7 by

$$-0.036,\quad -0.036,\quad 0.077,\quad \text{and}\quad 0.029\ cm^{-1},\ \text{respectively.}$$

The total calculated energy shifts are summarized in Table V.

V. ELECTROSTATIC MODELS FOR (X,Y) SPLITTINGS

A. (X,Y) splittings along the rare-earth series

The measured splittings of (X,Y) local-mode vibrations do not vary greatly along the R^{3+} series. For Ce^{3+} near the beginning of the R^{3+} series, the (X,Y) splitting for the H^-C_{4v} center in CaF_2 is 1.15 cm^{-1}. For Yb^{3+} near the end of the R^{3+} series, the (X,Y) splitting for the H^-C_{4v} center in CaF_2 is 0.70 cm^{-1}. This trend of similar splittings along the R^{3+} series contrasts with the predictions of the point-charge model. For Ce^{3+}, the point-charge model overestimates the (X,Y) splitting by a factor of more than two whereas for Yb^{3+}, the point-charge model under-estimates the (X,Y) splitting by a factor of 5.

Because of the quadratic dependence of the second-order perturbation electron-phonon interaction expressions on the $f_{\pm}$ terms of V_{ev}, any underestimates of these terms leads to large underestimates of the (X,Y) splittings. The underestimate of such electron-phonon terms by the point-charge model is particularly apparent at the lutecium end of the rare-earth series. The point-charge model involves the electron-phonon interaction parameters:

$$a_{1n}\langle r^n\rangle\alpha=\frac{eq\langle r^n\rangle}{4\pi\epsilon_0 D^{n+2}}\alpha,$$

which decrease along the rare-earth series (Table III). Because of the strong dependence of these electron-phonon parameters on the interionic distance D, the $n=2$ term gives the largest contribution, with the $n=4$ and $n=6$ terms having relatively minor effect.

The calculated (X,Y) splittings are sensitive to the host-lattice D value adopted. We cannot arbitrarily decrease D along the R^{3+} series because the measured crystal-field parameters decrease along the R^{3+} series. The problems with the point-charge model for the electron-phonon interaction are related to the equal lack of success of the point-charge model in estimating the axial crystal-field contributions of H^- ions of the H^-C_{4v} centers.

The point-charge values of the $n=2,4,6$ axial crystal-field parameters B_0^n for the contributions of a single point charge q located at distance D away from a R^{3+} ion of effective charge e is

$$B_0^n=\frac{eq\langle r^n\rangle}{4\pi\epsilon_0 D^3}.$$

There is a strong dependence of these parameters on the ionic separation D with the $n=2$ terms predominant. Nevertheless, it is well known from crystal-field fits that the $n=4$ and $n=6$ terms are of comparable magnitude and must be included.

On the point-charge model, the electron-phonon terms $a_{1n}\langle r^n\rangle\alpha$ are related to the crystal-field parameters B_0^n by

$$a_{1n}\langle r^n\rangle\alpha=\frac{eq\langle r^n\rangle}{4\pi\epsilon_0 D^{n+2}}\alpha=\frac{\alpha}{D}B_0^n.$$

Not all of the axial crystal-field contributions of the H^-C_{4v} centers can be attributed to the H^- ion alone. The introduction of the H^- charge-compensating ion causes some displacement of the surrounding F^- ions from cubic symmetry.[27] Nevertheless, the fourth and sixth-degree electron-phonon parameters need to be scaled up to reflect the crystal-field parameter trends. A full scaling up leads to a large over-estimate of the electron-phonon terms, which is accentuated by the quadratic dependence of the (X,Y) splittings on these terms. With partial scaling up of the $n=4$ and 6 electron-phonon terms, the point-charge model of the electron-phonon interaction can account for the observed magnitudes of the (X,Y) splittings.

In addition to point-charge effects, there are associated electron-phonon interaction terms[4] involving the induced dipole moment p of the H^- ion. The dipole-moment model considers the electrostatic interaction between the dipole moment p of the hydrogenic ion and the charge q of the 4f electron.[4] The dipole model electron-phonon terms could provide contributions to the calculated (X,Y) splittings that are comparable to those of the point-charge model.

B. Conclusions

The electron local-mode phonon interaction can account for the observed (X,Y) local-mode splitting for Kramers rare-earth ions. While the simple point-charge model has difficulties in accounting for some of the measured (X,Y) splittings, it can be adapted to obtain a degree of quantitative success. Scaling up the electron-phonon interaction parameters to fully follow the measured crystal-field parameters over-estimates the (X,Y) splittings. It is concluded that the electron-phonon interaction is the origin of the observed (X,Y) splittings. Covalency effects would be expected to play an important role for estimates of the electron-phonon interaction parameters, as was found for the crystal-field parameters.

VI. ZEEMAN SPLITTINGS OF (X,Y) LOCAL-MODE LINES

A. First-order Zeeman matrix analysis

In Secs. III–V, it was shown that the electron-phonon interaction V_{ev} can account quantitatively for the observed splittings of the (X,Y) local-mode of H^-C_{4v} centers. In this section, it is described how the application of an external magnetic field is used to confirm the electron-phonon origin of the (X,Y) splittings and analyses of measured spectra are presented.

Two magnetic-field geometries were used. With the magnetic field along a $\langle 100\rangle$ direction, two distinct magnetic subsites are created from the three possible orientations of C_{4v} centers. These are a C_4 symmetry subsite with the magnetic field along the parent C_{4v}-symmetry axis and a C_S symmetry subsite with the magnetic field perpendicular to the parent C_{4v}-symmetry axis. The Zeeman spectra of these two magnetic subsites are superposed, often leading to complex splitting patterns. With the magnetic field along a $\langle 111\rangle$ direction, all magnetic subsites are of C_1 symmetry and are equally inclined to the magnetic field.

The magnetic field does not have any effect on H^- vibrational states and any observed shifts or splittings are solely from the Zeeman effect for the electronic part of the total vibronic wave function. The method adopted for calculating

these effects is to form the first-order perturbation matrix of the vibronic wave functions. This first-order matrix approach has already been outlined in brief conference reports.[13,14] It provides a quantitative interpretation of the observed magnetic-field splitting patterns. The zero-field electron-phonon splitting is a second-order perturbation effect, which does not significantly alter the vibronic wave functions, and is included in the matrix as a phenomenological parameter. The Zeeman interaction terms for the electronic part of the wave functions are nonzero between those wave functions having identical vibrational components.

The cases considered have the electronic level well isolated, with the only exception being the H^-C_{4v} center of $CaF_2:Er^{3+}$. As the interpretation of this particular center is complex, it will be detailed separately in Sec. VI C.

For Kramers ions, the electronic states of C_{4v} centers transform either as γ_6 or γ_7 irreps. As the Zeeman analysis for the (X,Y) vibronics is the same for either of these irreps, the notation of $\psi^{\pm}$ for either a γ_6 or γ_7 ground state is adopted. For the absence of a magnetic field, the $\Psi_6^{\pm}$ and $\Psi_7^{\pm}$ vibronic states are assigned energies of $-\Delta$ and Δ respectively. The zero-field (X,Y) splitting of 2Δ is thus included as an experimentally determined parameter. The sign of Δ could be inferred from the electron-phonon analyses of Sec. III, but is not relevant for the calculated Zeeman pattens described here.

When the external magnetic field is applied, additional parallel and perpendicular Zeeman terms (denoted by P and S respectively) must be included between states having the same vibrational components. The Zeeman matrix for Kramers ions is

	$\psi^-[+]$	$\psi^+[+]$	$\psi^-[-]$	$\psi^+-[+]$
$\psi^-[+]$	$-\Delta-P$			$S^\star$
$\psi^+[-]$		$-\Delta+P$	S	
$\psi^-[-]$		$S^\star$	$\Delta-P$	
$\psi^+[+]$	S			$\Delta+P$

where the Zeeman terms are given by

$$P=\mu_B B_z\langle\psi^+|M_0^{(1)}|\psi^+\rangle=\tfrac{1}{2}\mu_B g_\parallel B_z,$$

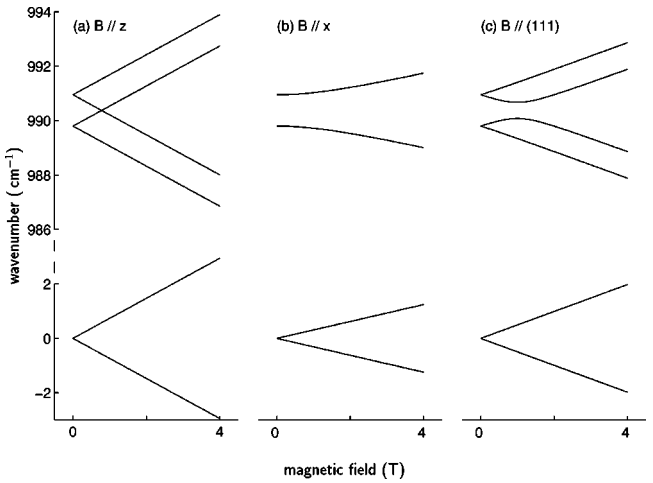

FIG. 2. Calculated energies of the ground and (X,Y) vibronic states of the H^-C_{4v} center of $CaF_2:Ce^{3+}$ as a function of magnetic field strength for magnetic fields applied: (a) parallel to the C_{4v} axis (C_4 subsite), (b) perpendicular to the C_{4v} axis (C_S subsite), and (c) parallel to the $\langle 111\rangle$ axis (C_1 site).

$$S=-\frac{1}{\sqrt{2}}\mu_B(B_x-iB_y)\langle\psi^+|M_1^{(1)}|\psi^-\rangle=\tfrac{1}{2}\mu_B g_\perp(B_x-iB_y),$$

where the $M_q^{(1)}$ are the spherical-basis components of $\mathbf{M}=\mathbf{L}+2\mathbf{S}$.

The Zeeman matrix for the splitting of the vibronic ground state $\psi^{\pm}(000)$ involves the same Zeeman terms, giving a linear Zeeman splitting for the Kramers-degenerate ground state.

1. Calculated Zeeman splittings of $H^-(X,Y)$ lines

The $\langle 100\rangle$ Zeeman spectra are a superposition of the spectra of the C_4 and C_S magnetic subsites, which have the magnetic field parallel and perpendicular to the parent C_{4v}-symmetry axis, respectively.

For the C_4 subsite, the two pairs of zero-field vibronic states do not mix, and the Zeeman splittings are linear and identical to the ground-state splitting as illustrated in Fig. 2(a) for the representative case of the H^-C_{4v} center of $CaF_2:Ce^{3+}$. Because the vibronic wave functions remain pure, the only transitions observed are those for which the initial and final electronic states have the same magnetic-field dependence and hence which produce no observed Zeeman shifts or splittings.

For the C_S magnetic subsite, the vibronic states do not each separately split in the field, but do mix with each other,

TABLE V. Measured and first- and second-order calculated shifts (in cm^{-1}) of the four vibronic states of the H^-C_{4v} center of Er^{3+} in CaF_2. The crystal-field contributions have been subtracted out.

Vibronic state	First order	Second order (First degree)	Second order (Second degree)	Total shift	Measured (± 0.1)
Φ_6^+	-0.190	-0.070	-0.036	-0.296	-0.61
Φ_7^+	-0.183	-0.064	-0.036	-0.283	-0.19
Ψ_6^+	0.840	-0.009	0.077	0.908	0.98
Ψ_7^+	0.833	-0.004	0.029	0.820	0.98

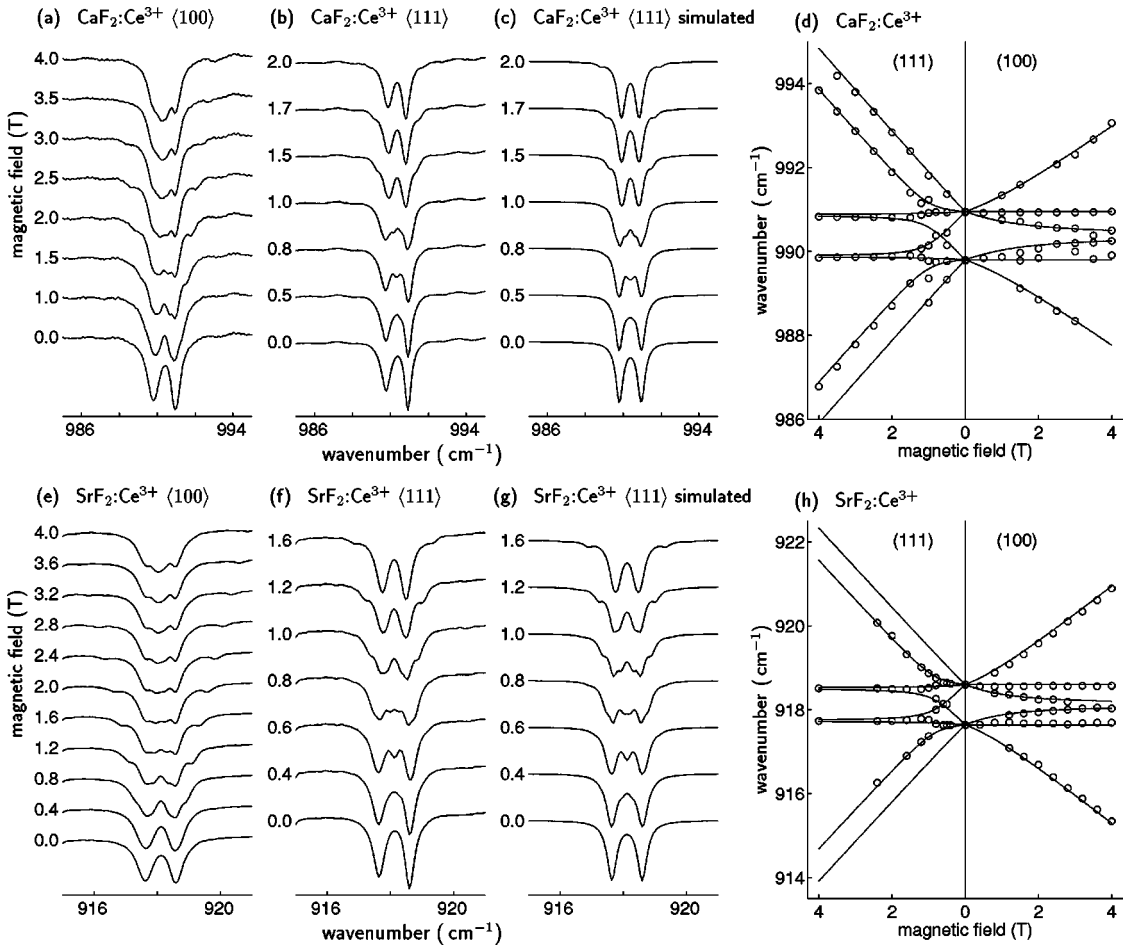

FIG. 3. 10 K measured and simulated infrared-absorption spectra of the (X,Y) vibronics, and derived Zeeman splitting diagrams, for H^-C_{4v} centers of $CaF_2:Ce^{3+}$ and $SrF_2:Ce^{3+}$. (a) $CaF_2:Ce^{3+}$ with $B\|\langle 100\rangle$. (b) $CaF_2:Ce^{3+}$ with $B\|\langle 111\rangle$. (c) Simulated spectra for $CaF_2:Ce^{3+}$ with $B\|\langle 111\rangle$. (d) Experimental and calculated Zeeman (X,Y) splitting patterns of $CaF_2:Ce^{3+}$ for $B\|\langle 111\rangle$ and $B\|\langle 100\rangle$. (e) $SrF_2:Ce^{3+}$ with $B\|\langle 100\rangle$. (f) $SrF_2:Ce^{3+}$ with $B\|\langle 111\rangle$. (g) Simulated spectra for $SrF_2:Ce^{3+}$ with $B\|\langle 111\rangle$. (h) Experimental and calculated Zeeman (X,Y) splitting patterns of $SrF_2:Ce^{3+}$ for $B\|\langle 111\rangle$ and $B\|\langle 100\rangle$.

giving an initial quadratic ''repulsion'' between them. In the high magnetic-field limit, this separation becomes identical to the linear splitting displayed by the ground state. This is illustrated in Figs. 2(b) for the case of the H^-C_{4v} center of $CaF_2:Ce^{3+}$. All four transitions of the C_S subsite have intensities that change as the mixing between the vibronic states changes.

For magnetic-fields in the $\langle 111\rangle$ direction, only one magnetic subsite exists, with C_1 symmetry. The calculated splittings are depicted in Fig. 2(c) for the case of the H^-C_{4v} center of $CaF_2:Ce^{3+}$. As all transitions are allowed, a pattern of up to eight lines is produced, again with intensities which change as the vibronic-state mixing changes.

Special cases of these Zeeman splittings arise for Sm^{3+} ions which have low $g_\|$ values and for Nd^{3+} and Dy^{3+} ions, which have low $g_\perp$ values.

2. Intensity analysis of (X,Y) lines of H^-C_{4v} centers

There is a large variation in intensities of the observed absorption lines which have been split by the Zeeman effect and this occurs for the following two reasons.

The pure local-mode vibrational transitions having no change in the electronic wave function component are electric-dipole allowed transitions very much more stronger than vibronic transitions in which both the the vibrational and electronic parts change. Specifically, transitions such as $\psi^+(000)\rightarrow\psi^+(100)$ are much stronger than transitions such as $\psi^+(000)\rightarrow\psi^-(100)$.

The relative thermal populations of the ground-state Zeeman sublevels alter the relative line intensities and these change with applied field.

The vibronic intensities can be modeled by considering the extent of mixing of vibronic states of the first-order Zeeman matrix. The strengths of the transitions are determined by the particular linear combinations that are the eigenfunctions of the first-order Zeeman matrix. Taking the limiting case for this intensity analysis, the equal strengths of the $\psi^+\rightarrow\psi^+$ and $\psi^-\rightarrow\psi^-$ transitions were set as unity, while the ''cross'' transitions $\psi^+\leftrightarrow\psi^-$ were set to zero intensity. The weighting of the transition strengths by the Boltzmann populations of their respective ground states is also included, although this has much less effect than the mixing of the wave functions.

For the $\langle 100\rangle$ Zeeman spectra, the relative weightings of the C_4 and C_S subsites adds an adjustable parameter since the relative strengths of the π and σ components of the

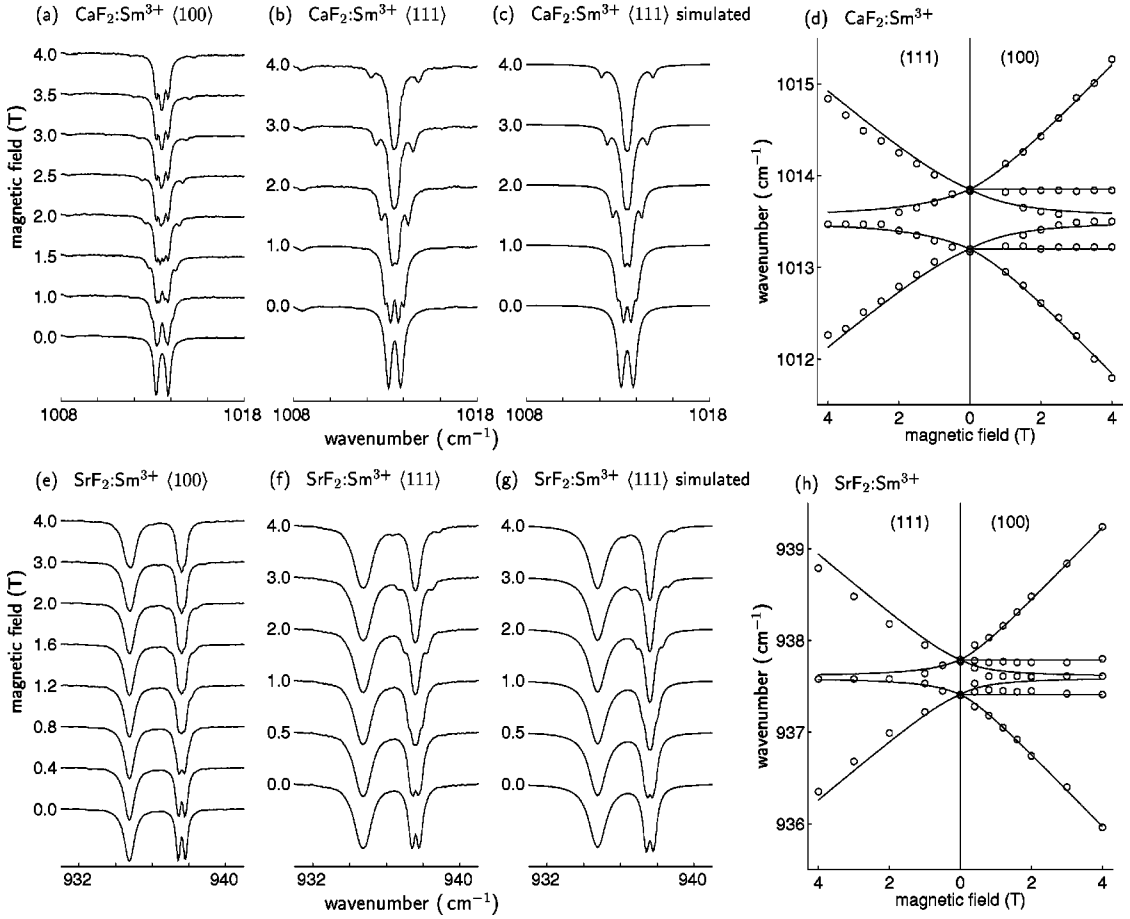

FIG. 4. 10 K measured and simulated infrared-absorption spectra of the (X,Y) vibronics, and derived Zeeman splitting diagrams, for H^-C_{4v} centers of CaF_2:Sm^{3+} and SrF_2:Sm^{3+}. (a) CaF_2:Sm^{3+} with B$\|\langle 100\rangle$. (b) CaF_2:Sm^{3+} with B$\|\langle 111\rangle$. (c) Simulated spectra for CaF_2:Sm^{3+} with B$\|\langle 111\rangle$. (d) Experimental and calculated Zeeman (X,Y) splitting patterns of CaF_2:Sm^{3+} for B$\|\langle 111\rangle$ and B$\|\langle 100\rangle$. (e) SrF_2:Sm^{3+} with B$\|\langle 100\rangle$. (f) SrF_2: Sm^{3+} with B$\|\langle 111\rangle$. (g) Simulated spectra for SrF_2:Sm^{3+} with B$\|\langle 111\rangle$. (h) Experimental and calculated Zeeman (X,Y) splitting patterns of SrF_2:Sm^{3+} for B$\|\langle 111\rangle$ and B$\|\langle 100\rangle$.

transition moments are not known. For the $\langle 111\rangle$-Zeeman spectra, with one magnetic subsite, this correction does not arise and the transition intensities can be modelled unambiguously.

B. Zeeman splitting of (X,Y) vibronics of H^-C_{4v} centers in CaF_2 and SrF_2

The Zeeman splittings of the R^{3+}-$H^-(X,Y)$ vibronic lines were measured for magnetic fields up to 4 T.

CaF_2:Ce^{3+} and SrF_2:Ce^{3+}

The $\langle 100\rangle$ and $\langle 111\rangle$ Zeeman splittings of the (X,Y) lines in CaF_2:Ce^{3+} [Figs. 3(a) and 3(b)] and SrF_2:Ce^{3+} [Figs. 3(e) and 3(f)] match the calculated energies well [Figs. 3(d) and 3(h)]. The $\langle 111\rangle$ simulated spectra correspond well with experiment [Figs. 3(c) and 3(g)], validating the intensity analysis of Sec. VI A 2.

CaF_2:Nd^{3+}, SrF_2:Nd^{3+}, and CaF_2:Dy^{3+}

For CaF_2:Nd^{3+} and SrF_2:Nd^{3+}, and for CaF_2:Dy^{3+}, the infrared-absorption spectra are not significantly changed when $\langle 111\rangle$ magnetic fields of up to 4 T are applied. In each of these cases, the parallel Zeeman effect dominates over the perpendicular effect. This results in a low level of mixing between the states causing the transitions that split away from the zero-field energies to have immeasurably low intensities. Simulated spectra for $\langle 111\rangle$ magnetic fields confirm this behavior.

CaF_2:Sm^{3+} and SrF_2:Sm^{3+}

The $\langle 100\rangle$ and $\langle 111\rangle$ Zeeman splittings of the (X,Y) lines in CaF_2:Sm^{3+} [Figs. 4(a) and 4(b)] and SrF_2:Sm^{3+} [Fig. 4(e) and 4(f)] match the calculated energies well [Figs. 4(d) and 4(h)] and, again, the intensities of the $\langle 111\rangle$ simulated spectra correspond very well with experiment [Figs. 4(c) and 4(g)].

The low value of $g_\|$ greatly simplifies the $\langle 111\rangle$-Zeeman spectra. The splitting in a $\langle 111\rangle$ magnetic field of the two vibronic states $\Psi_6^\pm$ and $\Psi_7^\pm$ is entirely due to the perpendicular component of the field, making the $\langle 111\rangle$ splittings identical to those for the C_S subsite of the $\langle 100\rangle$ orientation, but with the magnetic field scaled by $1/\sqrt{3}$.

The $\langle 100\rangle$-Zeeman diagram of superposed C_4 and C_S subsite splittings is not affected by the value of $g_\|$, since the only transitions observed for the C_4 subsite are unshifted in energy and this splitting pattern is similar to the Ce^{3+} case.

The longitudinal Z mode is also present in the spectra of SrF_2:Sm^{3+}. The Zeeman splitting confirms the assignment of the (X,Y) mode to the higher energy pair. The Z mode eigenfunction remains essentially pure with the result that no

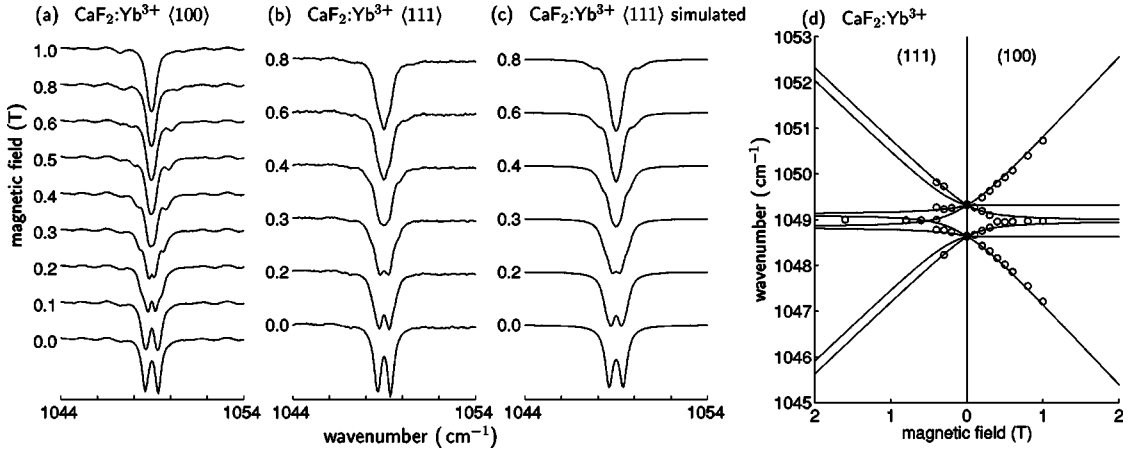

FIG. 5. 10 K measured and simulated infrared-absorption spectra of the (X,Y) vibronics, and derived Zeeman splitting diagrams, for H^-C_{4v} centers of CaF_2:Yb^{3+}. (a) CaF_2:Yb^{3+} with B$\|\langle 100\rangle$. (b) CaF_2:Yb^{3+} with B$\|\langle 111\rangle$. (c) Simulated spectra for CaF_2:Yb^{3+} with B $\|\langle 111\rangle$. (d) Experimental and calculated Zeeman (X,Y) splitting patterns of CaF_2:Yb^{3+} for B$\|\langle 111\rangle$ and B$\|\langle 100\rangle$.

splitting is observed, as for the (X,Y) mode in the C_4 subsite.

CaF_2:Gd^{3+}

The absence of resolvable zero-field (X,Y) splittings immediately puts any Zeeman effects that produce measureable splittings of the order of the experimental linewidth into the high-field regime, where any transitions away from zero-field energy have very low intensity.

CaF_2:Yb^{3+}

Broader lines result from a higher required level of H^- doping to offset the reduction of Yb^{3+} ions. In addition, the relatively large $g_\perp$ value causes the intensities of the outer transitions to drop rapidly for any applied magnetic field. The infrared spectra are shown in Figs. 5(a) and 5(b) for applied $\langle 100\rangle$ and $\langle 111\rangle$ magnetic fields. The simulated $\langle 111\rangle$ spectra [Fig. 5(c)] match the experimental spectra well with the energy splittings following the predicted behavior [Fig. 5(d)].

C. Zeeman splittings of the (X,Y) vibronics of H^-C_{4v} centers of CaF_2:Er^{3+}

The H^-C_{4v} center of CaF_2:Er^{3+} has a first excited state 4.5 cm^{-1} above the ground state which is significantly populated at 10 K. This state has to be included in any first-order electron-phonon matrix, thus introducing additional first-order contributions to the zero-field electron-phonon interaction (X,Y) splitting. The presence of this nearby state produces far more complex Zeeman splittings than were observed or calculated for any of the other Kramers ions.

The $\langle 111\rangle$-Zeeman spectra are displayed in Fig. 6(a). In calculating the Zeeman effect of these vibronic states, the first-order electron-phonon interaction matrix is extended to include the Zeeman interaction. Using the notation adopted in Sec. IV B, the combined electron-phonon and Zeeman interaction matrix for the eight vibronic states is

	$\phi^-[+]$	$\phi^+[-]$	$\phi^-[-]$	$\phi^+[+]$	$\psi^-[+]$	$\psi^+[-]$	$\psi^-[-]$	$\psi^+[+]$
$\phi^-[+]$	E_1-P_1			$S_1^\star$			$A-B$	$S_3^\star$
$\phi^+[-]$		E_1+P_1	S_1				$S_3^\star$	$A-B$
$\phi^-[+]$		$S_1^\star$	E_2-P_1		$A+B$	S_3		
$\phi^+[+]$	S_1			E_2+P_1	$S_3^\star$	$A+B$		
$\psi^-[+]$			$A+B$	S_3	E_3-P_2			$S_2^\star$
$\psi^+[-]$			$S_3^\star$	$A+B$		E_3+P_2	S_2	
$\psi^-[-]$	$A-B$	S_3				$S_2^\star$	E_4-P_2	
$\psi^+[+]$	$S_3^\star$	$A-B$			S_2			E_4+P_2

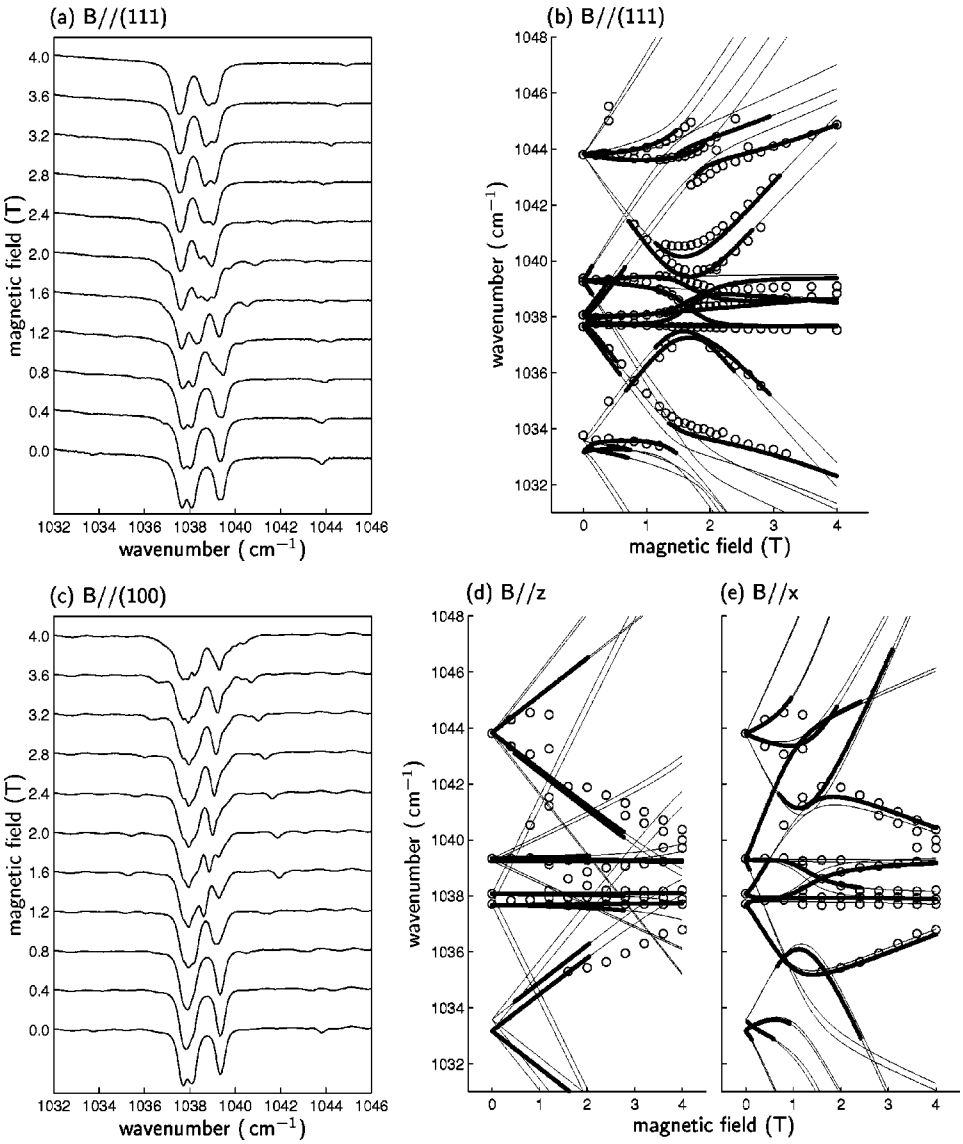

FIG. 6. 10 K infrared-absorption spectra of the (X,Y) vibronics for H^-C_{4v} centers of Er^{3+} in CaF_2. (a) Measured spectrum of CaF_2:Er^{3+} with $B\|\langle 111\rangle$. (b) Measured and calculated Zeeman splitting patterns for $B\|\langle 111\rangle$. (c) Measured spectrum of CaF_2:Er^{3+} with $B\|\langle 100\rangle$. (d) Measured and calculated Zeeman splitting patterns for magnetic fields parallel to the C_4 symmetry axis of the H^-C_{4v} center. (e) Measured and calculated Zeeman splitting patterns for magnetic fields perpendicular to the C_4 symmetry axis of the H^-C_{4v} center.

where $A\pm B$ are electron-phonon interaction terms, the E_i terms incorporate both crystal-field and electron-phonon interaction parts, and the Zeeman terms are

$$P_1=\mu_B B_z\langle\phi^+|M_0^{(1)}|\phi^+\rangle=\tfrac{1}{2}\mu_B g_\parallel^{\phi}B_z,$$

$$P_2=\mu_B B_z\langle\psi^+|M_0^{(1)}|\psi^+\rangle=\tfrac{1}{2}\mu_B g_\parallel^{\psi}B_z,$$

$$S_1=-\frac{1}{\sqrt{2}}\mu_B(B_x-iB_y)\langle\phi^+|M_1^{(1)}|\phi^-\rangle$$

$$=-\frac{1}{2}\mu_B g_\perp^{\phi}(B_x-iB_y),$$

$$S_2=-\frac{1}{\sqrt{2}}\mu_B(B_x-iB_y)\langle\psi^+|M_1^{(1)}|\psi^-\rangle$$

$$=\frac{1}{2}\mu_B g_\perp^{\psi}(B_x-iB_y),$$

$$S_3=-\frac{1}{\sqrt{2}}\mu_B(B_x-iB_y)\langle\psi^-|M_1^{(1)}|\phi^+\rangle$$

$$=-\frac{1}{2}\mu_B g_\perp^{\dagger}(B_x-iB_y),$$

where the $M_q^{(1)}$ are the spherical-basis components of $\mathbf{M}=\mathbf{L}+2\mathbf{S}$ and the g-value $g_\perp^{\dagger}$ required for the S_3 term was estimated as 4.41 from the calculated wave functions.

The electron-phonon terms are introduced as parameters, the E_i's absorbing the second-order shifts. The $A \pm B$ electron-phonon terms play a large part in determining the mixing of states in a magnetic field and must be included in the Zeeman analysis.

The matrix for the ground states includes the same Zeeman terms and the ground state splitting, E_0,

	$\phi^-(000)$	$\phi^+(000)$	$\psi^-(000)$	$\psi^+(000)$
$\phi^-(000)$	$-P_1$	$S_1^\star$		S_3
$\phi^+(000)$	S_1	P_1	$S_3^\star$	
$\psi^-(000)$		S_3	E_0-P_2	$S_2^\star$
$\psi^+(000)$	$S_3^\star$		S_2	E_0+P_2

It was found in the electron-phonon analysis of Sec. IV B that the second-degree electron-phonon terms estimated from the point-charge model were too small to account for the zero-field (X,Y) splittings. The $A \pm B$ parameters in this Zeeman matrix are thus truly parameters in that their values have not been determined by the zero-field splitting. They need to be scaled in magnitude to give the splittings which best approximate the measured data. To have just one parameter to adjust, the ratio A/B was held at the value given by the point charge model.

Calculation of the transition energies by diagonalization of these two matrices gives 32 possible transitions. The splitting diagram of these transitions will be far more complicated than could possibly be resolved using the available 0.1 cm^{-1} resolution. An indication of which transitions are expected to dominate the splitting diagram can be obtained by calculating intensities in a similar way as with the other Kramers ions.

Attempts to produce full simulated spectra for the $\langle 111 \rangle$ Zeeman patterns have not been successful. The presence of the extra electron-phonon interaction terms $A \pm B$ introduce parameters whose values could only be deduced by trial and error to produce the best simulated spectra. While the combined Zeeman and electron-phonon interaction matrix produces an appropriate pattern, mismatches are still significant. Even small mismatches lead to very different simulated and measured spectra.

The experimental and calculated splitting patterns are plotted in a splitting diagram in Fig. 6(b). As an intermediate stage to a full simulation of the spectra, those transitions calculated to gave high intensity have been plotted as bold lines.

The calculated intensities depend on the admixture of the vibronic wave functions and on the Boltzmann populations of the ground states. The criteria for inclusion of calculated lines as ''high intensity'' were adjusted to match the presence of experimental data as closely as possible. A transition was plotted as a bold line if (a) the magnitude of the admixture of the electronic wave functions was $\geqslant 0.1$ and if (b) the initial state had a thermal population of greater than 14%.

This splitting diagram demonstrates that the first-order Zeeman analysis can give a reasonable estimate of the Zeeman transition energies and an indication of their relative intensities.

$\langle 100 \rangle$-Zeeman patterns were also measured [Fig. 6(c)]. These $\langle 100 \rangle$-Zeeman patterns are more complicated than the $\langle 111 \rangle$-Zeeman patterns because of the superposition of the spectra of C_4 and C_S subsites. The peaks measured from these Zeeman spectra are plotted in Figs. 6(d) and 6(e) for the two magnetic subsites C_4 and C_S, with the calculated energies plotted as bold lines for the high-intensity transitions. The intensity criteria adopted do not accurately predict the observed transitions. However, the plots do account for the energies of those transitions which were observed.

It appears that the Zeeman lines of the C_4 subsite dominate over those of the C_S subsite for transition which have split away from the zero-field energies. This is consistent with the mixing between states being less for the C_4 subsite, which is only mixed by the electron-phonon interaction term, whereas for the C_S subsite, mixing is affected also by the Zeeman interaction.

VII. CONCLUSION

The splitting of the (X,Y) vibrational mode of the H^- ion in the R^{3+}-H^- C_{4v} sites in CaF_2 has been shown to be due to the electron-local mode phonon interaction. The point-charge model for this interaction has been used to estimate the magnitudes of the splitting for the Kramers R^{3+} ions and demonstrates that the interaction is of an appropriate magnitude to produce the observed splittings. As a second-order perturbation, the magnitude of the splitting is determined primarily by the proximity and nature of appropriate intermediate states.

The electron local-mode phonon interaction model was further tested by Zeeman measurements of the H^- local mode infrared absorption lines for these Kramers ions, with good agreement between the measured and simulated spectra. It sufficed to take the measured (X,Y) splittings and the R^{3+} ground state g values as known quantities to fit the Zeeman patterns. The Zeeman effects could then be quantitatively accounted for using zero-order electronic-vibrational coupled wave functions without introducing any additional parameters.

ACKNOWLEDGEMENTS

This research was supported by the University of Canterbury and the New Zealand Lottery Board. We wish to thank Ross Ritchie and Wayne Smith for technical assistance.

*Present address: Industrial Research, P.O. Box 31-310, Lower Hutt, New Zealand.
[1] R. A. Satten, D. R. Johnston, and E. Y. Wong, Phys. Rev. **171**, 370 (1968).
[2] S. R. Pollack and R. A. Satten, Phys. Rev. B **9**, 4628 (1974).
[3] G. D. Jones, S. Peled, S. Rosenwaks, and S. Yatsiv, Phys. Rev. **183**, 353 (1969).
[4] I. T. Jacobs, G. D. Jones, R. A. Satten, and K. Zdansky, Phys. Rev. B **3**, 2888 (1971).
[5] R. J. Reeves, G. D. Jones, and R. W. G. Syme, Phys. Rev. B **46**, 5939 (1992).
[6] T. P. J. Han, G. D. Jones, and R. W. G. Syme, Phys. Rev. B **47**, 14 706 (1993).
[7] K. Zdansky and A. Edgar, Phys. Rev. B **3**, 2133 (1971).
[8] K. M. Murdoch, G. D. Jones, and R. W. G. Syme, Phys. Rev. B **56**, 1254 (1997).
[9] A. Edgar, G. D. Jones, and M. R. Presland, J. Phys. C **12**, 1569 (1979).
[10] N. J. Cockroft, D. Thompson, G. D. Jones, and R. W. G. Syme, J. Chem. Phys. **86**, 521 (1987).
[11] N. J. Cockroft, G. D. Jones, and R. W. G. Syme, J. Chem. Phys. **92**, 2166 (1990).
[12] N. M. Strickland and G. D. Jones, Phys. Rev. B **56**, 10 916 (1997).
[13] G. D. Jones and N. M. Strickland, J. Lumin. **66&67**, 253 (1996).
[14] G. D. Jones, J. Lumin. **58**, 20 (1994).
[15] A. Edgar, C. A. Freeth, and G. D. Jones, Phys. Rev. B **15**, 5023 (1977).
[16] F. G. Wakim, M. Synek, P. Grossgut, and A. DaMommio, Phys. Rev. A **5**, 1121 (1972).
[17] I. J. Ashburner, R. C. Newman, and S. D. McLaughlan, Phys. Lett. **27A**, 212 (1968).
[18] A. Kafri, D. Kiro, S. Yatsiv, and W. Low, Solid State Commun. **6**, 573 (1968).
[19] J. M. Baker, W. Hayes, and D. A. Jones, Proc. Phys. Soc. London **73**, 942 (1959).
[20] R. K. Luks, I. G. Saitkulov, and A. L. Stolov, Fiz. Tverd. Tela (Leningrad) **11**, 261 (1969) [Sov. Phys. Solid State **11**, 210 (1969)].
[21] H. Nara and M. Schlesinger, J. Phys. C **5**, 606 (1972).
[22] A. Sivaram, H. Jagannath, R. D. Ramachandra, and P. Venkateswarlu, J. Phys. Chem. Solids **40**, 1007 (1979).
[23] R. W. Bierig and M. J. Weber, Phys. Rev. **132**, 164 (1963).
[24] A. A. Antipin *et al.*, Opt. Spectrosc. **33**, 372 (1971).
[25] M. Mujaji, G. D. Jones, and R. W. G. Syme, Phys. Rev. B **46**, 14 398 (1992).
[26] D. N. Chambers and R. C. Newman, Phys. Status Solidi **35**, 685 (1969).
[27] D. Kiro and W. Low, in *Magnetic Resonance*, edited by C. K. Coogan *et al.* (Plenum, London, 1970).
[28] C. A. Freeth, G. D. Jones, and R. W. G. Syme, J. Phys. C **15**, 5667 (1982).
[29] J.-P. R. Wells, Ph.D. thesis, University of Canterbury, 1997.
[30] J. Kirton and S. D. McLaughlan, Phys. Rev. **155**, 279 (1967).
[31] J. M. Baker and W. B. J. Blake, Proc. R. Soc. London, Ser. A **316**, 63 (1970).
[32] A. A. Antipin, I. N. Kurkin, G. K. Chirkin, and L. Y. Shekun, Fiz. Tverd. Tela (Leningrad) **6**, 2014 (1964) [Sov. Phys. Solid State **6**, 1590 (1965)].
[33] M. R. Brown, H. Thomas, J. S. S. Whiting, and W. A. Shand, J. Chem. Phys. **50**, 881 (1969).
[34] R. C. Newman and R. J. Woodward, J. Phys. C **7**, L432 (1974).